

# Dual-channel Geometric Registration of a Multispectral-augmented Endoscopic Prototype

O. Zenteno<sup>1</sup>, A. Krebs<sup>2</sup>, S. Treuillet<sup>1</sup>, Y. Lucas<sup>1</sup>, Y. Benezeth<sup>2</sup> and F. Marzani<sup>2</sup>

<sup>1</sup>PRISME, Université d'Orléans, F-45072 Orléans, France

<sup>2</sup>Le2i FRE2005, CNRS, Arts et Métiers, Univ. Bourgogne Franche-Comté, F-21000 Dijon, France

**Keywords:** Gastroendoscopy, Multispectral Imaging, Optical Biopsy.

**Abstract:** Multispectral measurement and analysis have proven to be useful to detect and monitor gastric pathologies at early stages. We developed a multispectral-augmented endoscopic prototype which allows exploration in the visible and near infrared range (400-1000 nm), increasing the common number of bands under analysis. The prototype comprises a fiberoptic connected to two multispectral snapshot cameras which is inserted through the instrument channel of a commercial endoscope. However, due to aseptic practices, the system must be sterilized between exams, forcing physicians to remove and reintroduce it on each examination and leading to different relative positions between modalities. In the present work, we introduce an axial displacement correction function for dual-channel registration (i.e., RGB and multispectral) based on the insertion depth of the fiberoptic. The performance was assessed using a chessboard pattern and its corner coordinates as ground truth. The mean RMSE error of the control points after registration using our method was  $2.3 \pm 0.7$  pixels, whereas the RMSE error using a frame by frame homographic registration was  $1.2 \pm 0.4$  pixels. In addition, the technique was tested on mouth exploration samples to simulate in-vivo acquisition. The results reveal that our method provides similar results when compared to a homographic transformation which would be impossible to perform in-vivo.

## 1 INTRODUCTION

Gastric inflammation is an invariable finding in patients infected with *Helicobacter pylori* and represents the host immune response to the organism. It produces surface epithelial degeneration and infiltration of the gastric mucosa by acute and chronic inflammatory cells. The prompt detection and diagnosis of gastric inflammation enables the initiation of early-stage therapy and can significantly increase the treatment quality among patients who develop further complications.

Current endoscopic systems can provide radially distorted RGB images of the stomach wall. However, spectral measurement and analysis, which provide accurate quantifications of morphology and microvasculature, are better to detect and monitor the progression of these pathologies at an early stage. Several commercial multispectral imaging approaches have been proposed to improve gastric exploration. Typical examples are Fuji Intelligent Chromo Endoscopy (FICE), proposed by Fuji and Narrow Band Imaging (NBI), proposed by Olympus (Song et al.,

2008). These techniques have shown the benefits of using multiple wavelengths for diagnosis. However they are limited in the number of wavelengths processed. We believe that using a larger number of bands in the visible and near infrared (400-1000 nm) could improve gastro-endoscopic exploration and diagnosis.

The common standard in the literature for in- and ex-vivo multispectral exploration is the use of filter wheels or push broom systems, respectively. However, both systems are ineffective for mapping moving inflamed areas due to the temporal lag between wavelengths. In contrast, snapshot multispectral systems can easily acquire reflectance data from the same area in all wavelengths simultaneously. The downside of this type of systems is their low resolution which extends into small scanning areas. Therefore, it is reasonable to believe that a larger frame of reference in the image is needed. Moreover, the majority of endoscopic systems are built-in with an instrument channel into which different tools (i.e., biopsy sampler, clamp tool, etc.) can be inserted. This makes it possible to insert a fiberoptic into this instrument channel. However both modalities need to be post-processed and regis-

tered in order to provide medically relevant information. This is not a trivial task, since due to the aseptic practices during medical and surgical procedures, the fiberscope must be sterilized between exams, forcing the physician to remove and reintroduce the fiberscope into the instrument channel on each examination. The procedure leads to different relative positions between the fiberscope and endoscope for each new video.

In addition, it is impossible to estimate the relation between coordinate systems using calibration patterns before the insertion of the fiberscope because, during the medical examination, the physician introduces first the endoscope into the patient for exploration and then the fiberscope into the instrument channel for localized screening. Thus, registration cannot be performed with conventional approaches (e.g., by matching singular points). Moreover, once the probe is inside the patient, the relative position between the two sensors is not fixed. In fact, two sources of relative movement are present: rotation and insertion. Rotation can be neglected if the introduction of the fiberscope into the endoscope is controlled so as to be performed always in the same position. However, the physician continuously inserts and retracts the fiberscope during exploration making it necessary to estimate a real time relation between the two sensors.

Nevertheless the end-tip of the fiberscope is visible throughout the endoscopic exploration. Therefore, it can be used as a feature for probe tracking if it is properly segmented. In the present work, we introduce an axial displacement correction function for the prototype of a multispectral-augmented endoscopic system based on the relative position between the two cameras. The prototype is intended to provide physicians with multispectral (MS) information in small regions of interest overlaid to endoscopic images with a wider range of vision. The remainder of this document is organized as follow: Section 2 summarizes current related work, Section 3 describes the system setup and its components, Section 4 presents the method, Section 5 the results obtained and finally Sections 6 and 7 the discussion and conclusion respectively.

## 2 RELATED WORK

In the gastrointestinal field, most multispectral and hyperspectral (HS) imaging studies have involved ex-vivo biopsies, resected tumor tissues, or organs such as the skin, tongue, or larynx. (Clancy et al., 2012) developed a laparoscopic HS system based on a liquid-crystal tunable filter (LCTF), (Martin et al., 2006)

and (Martin et al., 2012) developed an HS system with fluorescence for imaging of the larynx. (Dohi et al., 2005) used a micro Fabry-Perot interference filter placed at the tip of a flexible endoscope to create a wavelength-adjustable spectral endoscope. Nevertheless, this has not been used clinically yet. (Galeano et al., 2012) and (Kiyotoki et al., 2013), reported certain differences observed between healthy and pre-cancerous ex-vivo colon tissues. However, the color of the resected sampling tissues differed from what is normally observed in vivo, which suggests that the spectral properties of tissue may change after the resection process. In a recent study, (Martinez-Herrera et al., 2016) assessed the difference in the in vivo spectral response of malignant colorectal tumors and normal mucosa. Nevertheless, the acquisition systems used a color filter wheel, which makes temporal registration in different wavelengths a non-trivial task. Therefore, the main challenge we face is the registration between the different modalities (i.e. MS and RGB). Although some solutions for similar problems have been implemented in the past, they do not necessarily aim at quantitative measurements but rather to improve the visual perception of the surgeon to facilitate handling of the endoscope. For example: a non-tracked calibrated endoscope for 3D reconstruction and motion estimation from endo-nasal images was used in (Burschka et al., 2005) to register computerized tomography scans to the endoscopic video. Another navigation aid using photogrammetry during endoscopic surgery was studied in (Koppel et al., 2004). Here, structural information was used to prevent the endoscope image from flipping when the camera rotates. In (Westwood et al., 2004), the position of a marked tool inside the surgical scene was determined from laparoscopic images and used to create 3D renderings from different views for the surgeon. In (Deligianni, 2006), (Scholz et al., 1998), (Sauer et al., 2002) externally tracked cameras were used to augment the surgeon's view by fusing preoperative data with the actual endoscopic view. As mentioned before, none of them enhance the endoscopic image with MS information.

## 3 MULTISPECTRAL IMAGING PROTOTYPE

### 3.1 Experimental Setup

Figure 1 depicts a diagram of the flexible multispectral gastro-intestinal prototype, which can be used to obtain a series of reflected MS images in a con-

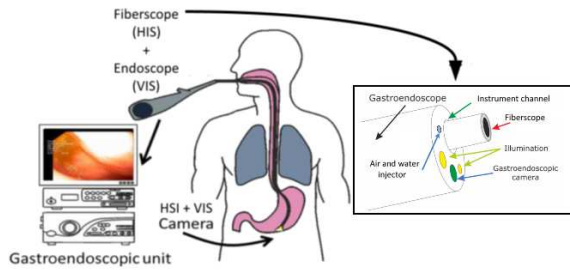


Figure 1: Concept diagram of the multispectral prototype.

tactless manner in the wavelength range of 470 to 975 nm.

The system comprises six units: a mercury (Xenon) light source, an endoscope imaging unit, a visible (VIS) range multispectral camera, a Near Infrared (NIR) range multispectral camera, a fiberscope and a twin-cam camera splitter. It was implemented as a modification of the commercialized Olympus (Tokyo, Japan) EVIS EXERA III endoscopic system by introducing an ITConcepts (Lahnau, Germany) microflex m2.5-2500 fiberscope in the instrument channel for dual simultaneous exploration. The fiberscope is connected at one side to a Cairn research (Kent, UK) TwinCam camera splitter by an optical adaptor and at the other to a mercury (Xenon) light source unit from Oriel Instruments (California, USA). Finally, the VIS range camera MQ022HG-IM-SM4X4-VIS and the NIR camera model MQ022HG-IM-SM5X5-NIR from Ximea (Munster, Germany) are connected to both ends of the splitter respectively. Figure 2 depicts the multispectral system including the light source, TwinCam system and fiberscope (left), the endoscopic system including the light source, processing system and endoscope (center) and an example of data acquisition using the prototype (right). The detailed specifications of the three cameras are presented in Table 1.

Table 1: Camera specification.

| Camera            | Resolution | Bands |
|-------------------|------------|-------|
| XIMEA SM5X5-NIR   | 409x216    | 25    |
| XIMEA SM4X4-VIS   | 512x256    | 16    |
| OLYMPUS EXERA III | 720x576    | 3     |

### 3.2 Acquisition Interface

A custom user interface was developed for data acquisition. The interface allows the user to capture the sequence of raw multispectral images and the gastroendoscopic video stream simultaneously. The three cameras must be connected to the computer. The endoscope is connected through a firewire interface and

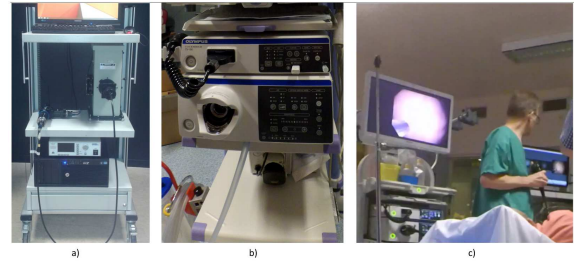


Figure 2: Experimental setup: (a) multispectral system, (b) endoscopic system, (c) in-vivo acquisition.

the multispectral cameras are connected via USB 3.0 interface. Currently the interface captures two images per second due to the exposure time required for the multispectral system. However, the interface is intended to be able to capture at the same frame rate as the endoscope (e.g., 25FPS). The complete processing pipeline of the images is currently done off-line (i.e., image matching, filtering, spectral analysis).

## 4 METHODS

To estimate the correction function and calibration of all the cameras at the same time, we used a common chessboard pattern of 17x15 squares of 1 mm. with an isosceles triangle in its center. The pattern allowed us to establish a relation between the geometrical coordinates of the two systems through a discrete measurement of how the triangle and its surroundings translate and expand in the image at different insertion depths. The proposed methodology is divided in five stages: Pre-processing, camera calibration, control point selection, parametric correction, and multispectral image enhancement. The first four are executed off-line and only once as part of a training phase. The last one can be executed independently, also off-line, at any time using the previously saved images.

The correction transformation ( $C_n$ ) where  $n$  is the selected frame can be formalized as a multiple sequential transformation matrix (as shown in Eq. (1)) composed by homographic ( $H_0$ ), scaling ( $S_n$ ) and translation ( $T_n$ ) transformations. ( $H_0$ ) is calculated only once during the training stage and is continuously used as the initial transformation at any depth.  $S_n$  and  $T_n$  are estimated for each frame and are linearly dependent on the detected insertion distance.

$$C_n = H_0 * S_n * T_n \quad (1)$$

$$C_n = \begin{bmatrix} h_{11} & h_{12} & h_{13} \\ h_{21} & h_{22} & h_{23} \\ h_{31} & h_{32} & h_{33} \end{bmatrix} \begin{bmatrix} s_x & 1 & 1 \\ 1 & s_y & 1 \\ 1 & 1 & 1 \end{bmatrix} \begin{bmatrix} 1 & 1 & t_x \\ 1 & 1 & t_y \\ 1 & 1 & 1 \end{bmatrix}$$

#### 4.1 Data Preprocessing

The raw images acquired from the multispectral sensors have to be preprocessed to remove noise and unwanted artifacts (i.e., the moire effect or honeycomb patterns) produced by the disposition of fibers. After acquiring sequential MS images containing different spectral information, we performed image preprocessing to reduce imperfections that arose during imaging and to generate images suitable for analysis. Noise reduction, contrast enhancement and illumination normalization were performed using common homomorphic filtering and de-vignetting techniques (Georgieva, 2015) and (Nair and Govindan, 2014).

#### 4.2 Dual Camera Calibration

Camera calibration is divided in two phases (i.e., spatial and spectral calibration). The first is applied before registration and the latter can be applied after registration for spectral data analysis. The spatial calibration was performed using MATLAB's built-in camera calibration toolbox which is a modified version of the method presented in (Bouquet, 2000). This method uses the pin-hole camera model. The initial estimation of the planar homographies is based on the method presented in (Zhang, 1999) and the closed-form estimation of the internal parameters was performed using orthogonality of vanishing points. The intrinsic model was similar to the one presented in (Heikkila and Silven, 1997). The spectral calibration was performed using a color matrix. With this matrix, a set of images with known spectral response was acquired to estimate the required linear transformation from raw data into real multispectral reflectance. A set of endoscopic and multispectral (fiberscope) images before and after geometrical correction are presented in Fig 3.

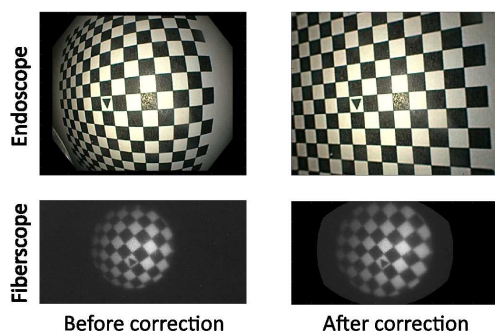


Figure 3: Endoscopic and fiberscopic images: Before (left) and after (right) radial distortion correction.

#### 4.3 Control Point Detection and Selection

The training homographic registration was performed using a initial grid of common points between the two undistorted modalities. The initial grid identification is executed in four steps; the complete process is depicted in Fig 4. First, an adaptive histogram equalization is applied on the pattern's image to enhance the dynamic range. Then, automatic thresholding and morphological operations are performed in order to obtain single Binary Large Objects (BLOB). After this, each BLOB is analyzed to find common characteristics to differentiate between triangles and rectangles (Number of vertices, extrema distribution and area relations). After identification of the central triangular pattern, the four proximate corners are identified based on their relative Euclidean distance. Finally, a new reference axis is defined based on the location of each triangle vertex.

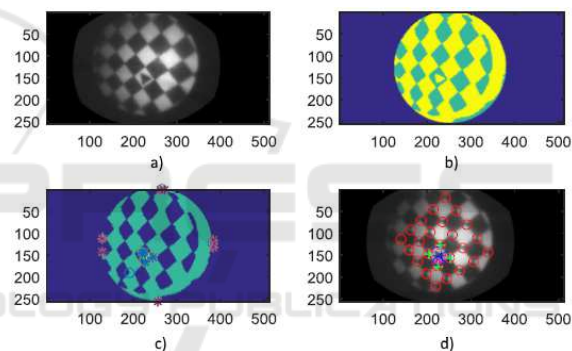


Figure 4: Pattern identification and creation of new axis on fiberscopic images. (a) Histogram equalization, (b) Thresholding, (c) BLOB analysis, (d) New reference axis centered in the triangle vertex.

After the new axial reference has been defined a common set of control points is identified in the two images. This is based on two-dimensional exploration of the point grid and intersection of coordinate points (as shown in Fig 5). The discrimination criteria consists in maximizing the number of common detected corners starting from the new origin and expanding to the four cardinal points of the new coordinate system.

The final projective transform matrix is calculated as the homography between the two set of coordinate points. Due to the different size and resolution of the images a new global coordinate system is applied to the scaled fiberscopic image.

#### 4.4 Parametric Correction Model

The estimation of the correction function is divided in two steps: Insertion measurement and estimation

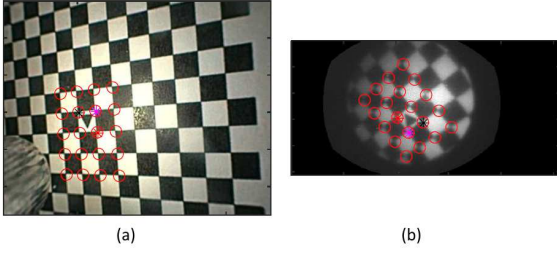


Figure 5: Common grid creation on the new axis on (a) endoscopic images, (b) fiberoptic images.

of the transformation matrix. Both steps are initially performed on a training set consisting of 15 endoscopic and 15 multispectral images, each one with the fiberoptic at a different insertion depth. To measure this depth during exploration the depth of the tip in the color images is tracked. As the present study focuses particularly on the relation between depth and transformation, we decided to perform manual segmentation of the fiberoptic tip to guarantee the highest measurement precision possible. Further segmentation techniques need to be explored after validation. The depth measurement procedure is depicted in Fig.6. First, the resulting BLOP from the segmentation is initially fitted to an ellipsoid and its two axes are calculated. The ellipsoid's horizontal axis is then projected into infinity. Finally, the Euclidian distance between the intersections of the projected line with the borders of the segmented BLOB and the left lateral limit of the image is measured in pixels.

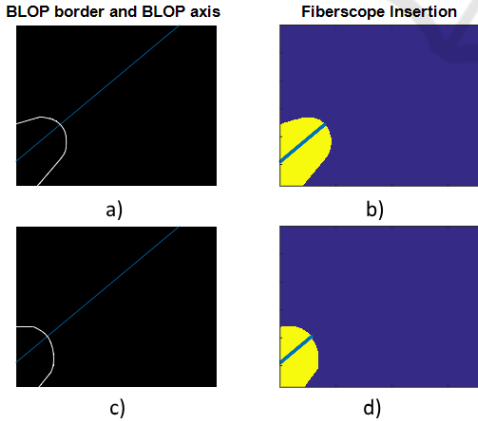


Figure 6: (a),(c): Segmentation of the fiberoptic tip and (b),(d): BLOP's axis intersection measurement.

For the transformation matrix estimation, we analyzed the mean of the distances from the center of the triangle to 8 points in the borders of the central 2x2 pattern on all the images in the data base. Fig 7. depicts the eight corners, the center of the pattern and the distance between each of them on a sample

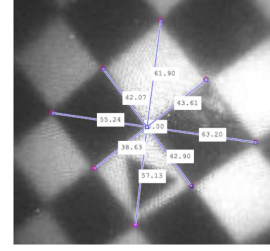


Figure 7: Measurement of distances to the center of the 2x2 central pattern.

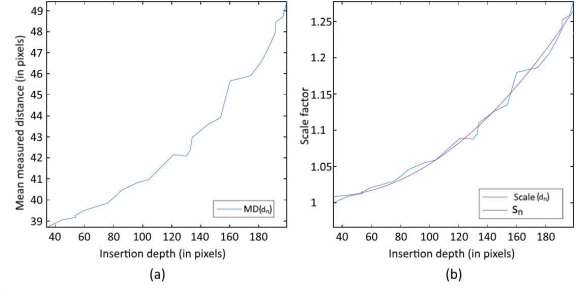


Figure 8: Relation graphs between insertion depth and: (a) mean measured distance, (b) normalized scaling factor.

fiberoptic frame. We used this information to evaluate the relation between the insertion depth and how the mean distance between corners and center scales through different frames. To estimate the scaling factor, a normalization of the measured distance based on the first sampling frame was performed. After this, a quadratic fit was applied to obtain a function of scaling based on depth (Fig. 8).

However, the central axis of the transformation was not always located in the center of the image. Therefore, the center of the displacement needed to be measured frame by frame based on the location of the center on the triangle from the pattern. This measurement was also compared to the insertion depth and fitted to a quadratic function corresponding to each axis. The corresponding functions for the x and y axes are shown in Fig. 9.

In addition, the scaling and translation correction functions (i.e.,  $s_n$ ,  $t_{x_n}$  and  $t_{y_n}$ ) are formalized as a function of the insertion depth ( $d_n$ ) as shown in Eq. (2),(3) and (4).

$$s_n = 8.8 \times 10^{-6} d_n^2 - 5 \times 10^{-4} d_n + 1 \quad (2)$$

$$t_{x_n} = 2 \times 10^{-3} d_n^2 - 9.4 \times 10^{-2} d_n + 0.52 \quad (3)$$

$$t_{y_n} = 1.5 \times 10^{-3} d_n^2 - 6.6 \times 10^{-2} d_n - 0.055 \quad (4)$$

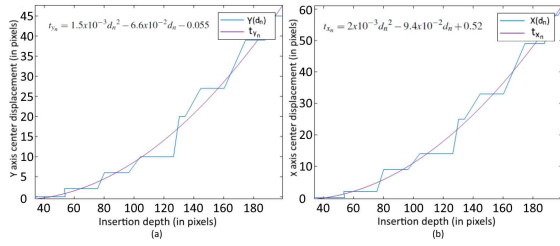


Figure 9: Relation graph between insertion depth and: (a) x-axis translation, (b) y-axis translation.

#### 4.5 Multispectral Enhancement

Finally, once the correction functions have been estimated the fiberscope-to-endoscope registered image  $I_r$  can be performed at any continuous point on the insertion depth range. This is done by replacing the values of the scaling and translation factor  $s_n$  and  $t_n$  obtained from Eq. (2), (3) and (4) in the correction transformation described in Eq. (1) and applying it to the original image  $I_o$  as follows:

$$\begin{bmatrix} x' \\ y' \\ 1 \end{bmatrix}_{I_r} = T_n * S_n * H_0 * \begin{bmatrix} x \\ y \\ 1 \end{bmatrix}_{I_o}, \text{ where} \quad (5)$$

$$S_n = \begin{bmatrix} s_n & 1 & 1 \\ 1 & s_n & 1 \\ 1 & 1 & 1 \end{bmatrix} \text{ and } T_n = \begin{bmatrix} 1 & 1 & t_{x_n} \\ 1 & 1 & t_{y_n} \\ 1 & 1 & 1 \end{bmatrix}$$

#### 4.6 Performance Assessment

The performance test was executed using a chessboard pattern as sample and the coordinates of its corners as ground truth. The test sample comprised 25 MS and endoscopic frames in which the fiberscope is at different insertion depths. The fiberscope is always observable in the endoscopic image. For evaluation, the mean RMSE error and standard deviation (when compared to the ground truth coordinates) on each corner of the pattern after registration with our method were compared to those obtained when using a frame-by-frame homographic registration. In addition, the registration was also tested on mouth exploration samples to simulate in-vivo acquisition. In all cases, the acquisition on all cameras was performed simultaneously

### 5 RESULTS

An example of the registration results is depicted on Fig. 10. Four different registered fiberscope and endoscope image overlays at a different position of

the fiberscope for each frame are shown. The endoscopic image appears in the background in a darker tone, while the transformed fiberscopic image appears highlighted. While observing the images it is easy to recognize the progressive transformation of the fiberscopic image at different depths.

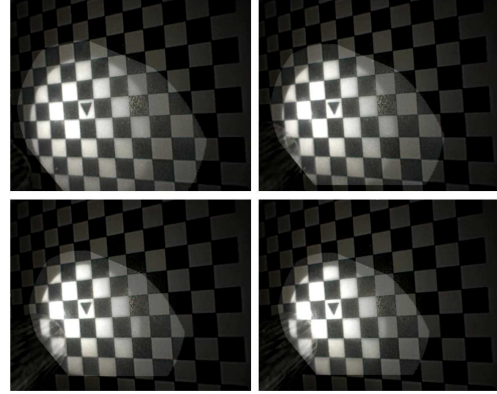


Figure 10: Examples of registered images where the fiberscope is at different depths.

Performance statistics for each set of images are presented in Table 2. The mean RMSE error between ground-truth coordinate points and the resulting transformed coordinates using frame-by-frame homography and our correction transformation matrix were  $1.2 \pm 0.4$  and  $2.3 \pm 0.7$  respectively.

In addition, the qualitative performance of the proposed method on mouth samples revealed a high level of coherence between the registered images. Figure 11 depicts a sample frame of the resulting video. The registered spectral information of a single wavelength and a frame of a mouth exploration endoscopic video are presented on the left and right of the image respectively. Although the data of a single band is not enough to characterize the tissue, the image illustrates the potential of the technique for in-vivo applications.



Figure 11: Qualitative results on in-vivo mouth samples.

### 6 DISCUSSION

The results are encouraging. Visually, the registered pattern fits seamlessly into the endoscopic image at different insertion depths. Statistically, the error in all cases was lower than 4 pixels. AS the resolution of

Table 2: Comparison of the performance of control point homography vs the proposed method.

| Frame | $H_n$ RMSE    | $C_n$ RMSE    |
|-------|---------------|---------------|
| 1     | 0.9           | 3.1           |
| 2     | 1.2           | 2.6           |
| 3     | 1             | 3.3           |
| 4     | 1             | 3.2           |
| 5     | 1.7           | 3.8           |
| 6     | 1.1           | 3.1           |
| 7     | 1.2           | 2.7           |
| 8     | 0.9           | 3.1           |
| 9     | 0.9           | 2.1           |
| 10    | 1.1           | 1.8           |
| 11    | 1.2           | 2.2           |
| 12    | 0.9           | 1.9           |
| 13    | 1.4           | 2.1           |
| 14    | 1.3           | 1.8           |
| 15    | 1.            | 2             |
| 16    | 0.8           | 2.5           |
| 17    | 1             | 1.7           |
| 18    | 2.3           | 2.5           |
| 19    | 1             | 2             |
| 20    | 2             | 1.7           |
| 21    | 1.2           | 1.5           |
| 22    | 1             | 1.2           |
| 23    | 1.5           | 1.7           |
| 24    | 1.1           | 1.1           |
| 25    | 1.2           | 1.9           |
| MEAN  | $1.2 \pm 0.4$ | $2.3 \pm 0.7$ |

the endoscopic images is 726x576p, a 2-3 pixel error is less than 1% on each direction. Moreover, the simplicity of the proposed pipeline and the use of common image processing tools make it ideal for future real-time implementations.

However, although the presented method has proven to effectively correct the difference between the relative position of the two camera axes, some limitations are still present. First, in the current implementation the insertion of the endoscope was controlled to ensure that it was always performed in the same position. Even though it is a trivial task, it would be ideal to relieve the physician of this constraint. The rotational problem can be easily solved by performing an affine transformation. However, we have not yet been able to identify a marker which can be used to measure the degrees required in the rotation. Secondly, we detected a third source of movement which we call precession that is produced by the circular movement of the fiberscope through the small surrounding space between the endoscope and the fiber. Further exploration of the effects of precession in a wider range of positions should be carried out. Thirdly,

the correction function will always be system dependent, this means that the initial discrete homography process should always be executed if the physician changes the endoscope or video system. However, if the video system is modified, a camera calibration is always required and the two processes (i.e., calibration and correction) can be performed simultaneously with similar data. Finally, the current frame rate of the multispectral system is two images per second. This may produce motion artifacts introduced by either the probe operator or target movement and is not ideal to perform in-vivo acquisitions. In contrast, the endoscopic video frame rate is much higher with the standard 25 images per second. Further development is being performed in the interface on a real-time implementation of these steps, which will not only overlaid single endoscope images but will also be able to show real time spectral information to physicians. Also, a real gastro-endoscopic sample is required for further exploration of the spectral data.

## 7 CONCLUSIONS

This paper has presented a method for compensation of the insertion and retraction motion of a fiberscope inserted in the instrument channel of an endoscope by using simple geometrical transformations. The technique relies on applying a linear affine transformation over a one-time control point homography. Manual segmentation of the fiberscope in the endoscopic images is performed for precise estimation of the position and orientation of the fiberscope camera. Experimental results using real endoscopic images showed that the method can track the camera insertion and retraction motion. Although the pipeline is currently executed off-line, this paper demonstrates the potential of image-based tracking of a fiberscope. The incorporation of more degrees of freedom in the proposed method may enable us to achieve real-time and robust tracking in the future.

## ACKNOWLEDGEMENTS

The authors would like to thank M.D. Dominique Lamarque, for his assistance in mouth data acquisition and endoscope handling. This work was supported by the EMMIE (Endoscopie MultiModale pour les lésions Inflammatoires de l'Estomac) project funded by the ANR-15-CE17-0015 grant.

## REFERENCES

- Bouguet, J.-Y. (2000). Matlab camera calibration toolbox. *Caltech Technical Report*.
- Burschka, D., Li, M., Ishii, M., Taylor, R. H., and Hager, G. D. (2005). Scale-invariant registration of monocular endoscopic images to ct-scans for sinus surgery. *Medical Image Analysis*, 9(5):413–426.
- Clancy, N. T., Stoyanov, D., James, D. R., Di Marco, A., Sauvage, V., Clark, J., Yang, G.-Z., and Elson, D. S. (2012). Multispectral image alignment using a three channel endoscope in vivo during minimally invasive surgery. *Biomedical optics express*, 3(10):2567–2578.
- Deligianni, F. (2006). *VIRTUAL AUGMENTATION FOR VIRTUAL ENVIRONMENTS IN SURGICAL TRAINING*. PhD thesis, Imperial College London.
- Dohi, T., Matsumoto, K., and Shimoyama, I. (2005). The micro fabry-perot interferometer for the spectral endoscope. In *Micro Electro Mechanical Systems, 2005. MEMS 2005. 18th IEEE International Conference on*, pages 830–833. IEEE.
- Galeano, J., Jolivot, R., Benezeth, Y., Marzani, F., Emile, J.-F., and Lamarque, D. (2012). Analysis of multispectral images of excised colon tissue samples based on genetic algorithms. In *Signal Image Technology and Internet Based Systems (SITIS), 2012 Eighth International Conference on*, pages 833–838. IEEE.
- Georgieva, V. (2015). Homomorphic filtering approach for narrowband images enhancement. *Journal of Applied Electromagnetism (JAE)*, in print.
- Heikkila, J. and Silven, O. (1997). A four-step camera calibration procedure with implicit image correction. In *Computer Vision and Pattern Recognition, 1997. Proceedings., 1997 IEEE Computer Society Conference on*, pages 1106–1112. IEEE.
- Kiyotoki, S., Nishikawa, J., Okamoto, T., Hamabe, K., Saito, M., Goto, A., Fujita, Y., Hamamoto, Y., Takeuchi, Y., Satori, S., et al. (2013). New method for detection of gastric cancer by hyperspectral imaging: a pilot study. *Journal of biomedical optics*, 18(2):026010–026010.
- Koppel, D., Wang, Y.-F., and Lee, H. (2004). Image-based rendering and modeling in video-endoscopy. In *Biomedical Imaging: Nano to Macro, 2004. IEEE International Symposium on*, pages 269–272. IEEE.
- Martin, M. E., Wabuye, M. B., Chen, K., Kasili, P., Panjehpour, M., Phan, M., Overholt, B., Cunningham, G., Wilson, D., DeNovo, R. C., et al. (2006). Development of an advanced hyperspectral imaging (hsi) system with applications for cancer detection. *Annals of biomedical engineering*, 34(6):1061–1068.
- Martin, R., Thies, B., and Gerstner, A. O. (2012). Hyperspectral hybrid method classification for detecting altered mucosa of the human larynx. *International journal of health geographics*, 11(1):21.
- Martinez-Herrera, S. E., Benezeth, Y., Boffety, M., Emile, J.-F., Marzani, F., Lamarque, D., and Goudail, F. (2016). Identification of precancerous lesions by multispectral gastroendoscopy. *Signal, Image and Video Processing*, 10(3):455–462.
- Nair, J. J. and Govindan, V. (2014). Intensity inhomogeneity correction using modified homomorphic unsharp masking. *Journal of Medical Imaging and Health Informatics*, 4(2):285–290.
- Sauer, F., Khamene, A., and Vogt, S. (2002). An augmented reality navigation system with a single-camera tracker: System design and needle biopsy phantom trial. *Medical Image Computing and Computer-Assisted Intervention MICCAI 2002*, pages 116–124.
- Scholz, M., Konen, W., Tombrock, S., Fricke, B., Adams, L., Von Duering, M., Hentsch, A., Heuser, L., and Harders, A. (1998). Development of an endoscopic navigation system based on digital image processing. *Computer Aided Surgery*, 3(3):134–143.
- Song, L. M. W. K., Adler, D. G., Conway, J. D., Diehl, D. L., Farraye, F. A., Kantsevov, S. V., Kwon, R., Mammula, P., Rodriguez, B., Shah, R. J., et al. (2008). Narrow band imaging and multiband imaging. *Gastrointestinal endoscopy*, 67(4):581–589.
- Westwood, J. et al. (2004). Reconstruction and enhancement in monocular laparoscopic imagery. *Medicine Meets Virtual Reality 12: Building a Better You: the Next Tools for Medical Education, Diagnosis, and Care*, 98:37.
- Zhang, Z. (1999). Flexible camera calibration by viewing a plane from unknown orientations. In *Computer Vision, 1999. The Proceedings of the Seventh IEEE International Conference on*, volume 1, pages 666–673. Ieee.